Carbon 144 (2019) 666–674

Contents lists available at ScienceDirect

Carbon

journal homepage: www.elsevier.com/locate/carbon

Gradients of microstructure, stresses and mechanical properties in a multi-layered diamond thin film revealed by *correlative cross-sectional nano-analytics*

David P. Gruber [a, b], Juraj Todt [b], Nicolas Wöhrl [c], Jakub Zalesak [b], Michael Tkadletz [d], Adam Kubec [e, 1], Sven Niese [f], Manfred Burghammer [g], Martin Rosenthal [g], Hadwig Sternschulte [h], Manuel J. Pfeifenberger [b], Bernhard Sartory [i], Jozef Keckes [a, b, *]

[a] *Department of Materials Physics, Montanuniversität Leoben, 8700, Leoben, Austria*
[b] *Erich Schmid Institute for Materials Science, Austrian Academy of Sciences, 8700, Leoben, Austria*
[c] *Faculty of Physics and CENIDE, University of Duisburg-Essen, Germany*
[d] *Department of Physical Metallurgy and Materials Testing, Montanuniversität Leoben, Leoben, Austria*
[e] *Fraunhofer IWS, Dresden, Germany*
[f] *AXO Dresden GmbH, Dresden, Germany*
[g] *European Synchrotron Radiation Facility, Grenoble, France*
[h] *Fakultät für Geistes- und Naturwissenschaften, Hochschule Augsburg, Augsburg, Germany*
[i] *Materials Center Leoben Forschung GmbH, 8700, Leoben, Austria*

ARTICLE INFO

Article history:
Received 31 October 2018
Received in revised form
20 December 2018
Accepted 23 December 2018
Available online 4 January 2019

ABSTRACT

Thin diamond films deposited by chemical vapour deposition (CVD) usually feature cross-sectional gradients of microstructure, residual stress and mechanical properties, which decisively influence their functional properties. This work introduces a novel *correlative cross-sectional nano-analytics approach*, which is applied to a multi-layered CVD diamond film grown using microwave plasma-enhanced CVD and consisting of a ~8 μm thick nanocrystalline (NCD) base and a ~14.5 μm thick polycrystalline (PCD) top diamond sublayers. Complementary cross-sectional 30 nm beam synchrotron X-ray diffraction, depth-resolved micro-cantilever and hardness testing and electron microscopy analyses reveal correlations between microstructure, residual stress and mechanical properties. The NCD sublayer exhibits a 1.5 μm thick isotropic nucleation region with the highest stresses of ~1.3 GPa and defect-rich nanocrystallites. With increasing sublayer thickness, a ⟨110⟩ fibre texture evolves gradually, accompanied by an increase in crystallite size and a decrease in stress. At the NCD/PCD sublayer interface, texture, stresses and crystallite size change abruptly and the PCD sublayer exhibits the presence of Zone T competitive grain growth microstructure. NCD and PCD sublayers differ in fracture stresses of ~14 and ~31 GPa, respectively, as well as in elastic moduli and hardness, which are correlated with their particular microstructures. In summary, the introduced nano-analytics approach provides complex correlations between microstructure, stresses, functional properties and deposition conditions.

1. Introduction

Due to their outstanding electronic, chemical, thermal, mechanical and biocompatible properties, diamond thin films have attracted significant scientific and technological attention in the last decades [1,2]. Polycrystalline diamond thin films produced by low-pressure chemical vapour deposition (CVD) nowadays represent one of the most common applications of synthetic diamond [3,4]. During the CVD process, a *complex cross-sectional microstructure* is usually formed in a sequence of growth stages including nucleation, coalescence and a final growth stage [2,5–10]. In addition, during both the growth process and the subsequent cooling down to room temperature, (intrinsic) growth and (extrinsic) thermal stresses accumulate in the films as a result of the

* Corresponding author. Department of Materials Physics, Montanuniversität Leoben, 8700, Leoben, Austria.
E-mail address: keckes@unileoben.ac.at (J. Keckes).
[1] Now at Paul Scherrer Institute, 5232 Villigen-PSI, Switzerland.

https://doi.org/10.1016/j.carbon.2018.12.093
0008-6223/

gradual microstructural evolution and the mismatch of coefficients of thermal expansion (CTEs) between the film and substrate, respectively [11–20]. The gradients of intrinsic stress can be very pronounced as a result of the gradual microstructure evolution, which may include an evolutionary selection of distinct crystallographic orientations, the development of columnar grain morphology, incorporation of non-diamond phases at grain boundaries, porosity, coalescence of grains, and/or the formation of twins and stacking faults [8,13,15].

Mechanical properties of CVD diamond thin films are strongly dependent on grain size, where, with increasing grain size, Young's moduli ~(400–1200 MPa) and hardness ~(40–110 GPa) tend to increase to a certain extent, whereas fracture stress ~(1–9 GPa) decreases [21–27]. The grain size also influences the surface roughness of the films and, in nanocrystalline diamond (NCD), smoother film surfaces occur due to the fact, that (i) surface roughness is decoupled from film thickness and (ii) better film homogeneity as well as isotropic material properties, compared to polycrystalline diamond (PCD), are present [4,26], [28]. The characterisation of mechanical properties of CVD diamond thin films has, however, been performed mainly by using indentation techniques [26,29,30], and three and four-point bending tests [31,32], which provide primarily surface and/or volume-average properties.

In contrast, the functional properties of CVD diamond films depend decisively on the cross-sectional gradients of microstructure and residual stress [15,26]. For example, residual stress gradients in CVD diamond films may induce unwanted bending of the film, when removed from the underlying substrate, *e.g.* to be applied in microelectromechanical systems. Therefore, the understanding of the correlation between cross-sectional microstructure and residual stress gradients on one side, and overall as well as depth-dependent mechanical properties on the other side, is of significant importance for the successful application of CVD diamond thin films.

The aim of this work is (i) to introduce a novel concept for the analysis of gradient CVD diamond thin films based on *correlative cross-sectional nano-analytics* including 30 nm cross-sectional X-ray nano-diffraction (CSnanoXRD) in conjunction with depth-resolved micromechanical testing and (ii) to discuss the correlation between gradients of microstructure, residual stress and mechanical properties in a model multi-layered CVD diamond film consisting of a NCD base and a PCD top sublayers. The novel nano-analytics approach opens new possibilities for the understanding of the correlation between (i) applied time-dependent process conditions, (ii) cross-sectional depth-dependent gradients of microstructure, residual stress and mechanical properties and (iii) overall functional properties of diamond thin films.

2. Experimental

2.1. Deposition of NCD/PCD diamond thin film

The diamond film was deposited by a microwave plasma-enhanced chemical vapour deposition (MPECVD) method (using a 2.45 GHz IPLAS CYRANNUS I plasma source) on a Si(100) wafer with a thickness of 425 μm. Prior to the deposition, the substrate was ultrasonically treated for 30 min with an abrasive solution consisting of diamond powder (20 nm grain size), Ti powder (5 nm particle size), and ethanol in a weight percent ratio of 1:1:100 (wt %). In a next step, the substrate was first ultrasonically cleaned for 15 min in acetone to remove any residue of the abrasive solution from the surface before the plasma cleaning was performed. Finally, the multi-layered 22.5 μm thick film consisting of 8 and 14.5 μm thick NCD and PCD sublayers, respectively, was deposited. The main process parameters are summarised in Table 1.

2.2. Synchrotron CSnanoXRD characterisation

A thin lamella with dimensions of ~(3×0.5) mm^2 and a thickness L of ~100 μm (in the X-ray beam direction, cf. Fig. 1) was prepared by mechanical thinning from the NCD/PCD film on Si(100). The sample was investigated by CSnanoXRD [33,34], at the ID13 nano-focus beamline of the European Synchrotron Radiation Facility in Grenoble, France. The experiment was performed in transmission geometry, using a pencil X-ray beam focussed by a Multi-layer Laue lens (MLL) to cross-sectional dimensions of ~15 μm × ~30 nm [34] and a photon energy of 13 keV (Fig. 1). The sample was moved in the X-ray beam with a constant step size of ~25 nm along the film normal direction using a piezo-actuated stage while the diffraction signal was recorded using a two-dimensional (2D) charged-coupled device detector (CCD) Eiger X 4M featuring a pixel size of 75×75 μm^2. To calibrate the powder diffraction experimental geometry, a NIST LaB_6 standard powder was measured at the same sample-to-detector distance as the diamond film sample. The collected Debye-Scherrer (DS) rings from the NIST sample were used to calibrate the sample-to-detector distance of 124.71 mm, the tilt angle of the detector plane of 0.85° and the rotation angle of the tilt plane of 152.42°, as well as the beam centre on the detector at 969.4 and 1182.8 pixels (in horizontal and vertical directions).

The DS rings collected from the diamond sample were processed using the Python package pyFAI [35]. Due to the relation of sample-to-detector distance to photon energy, there was only one diamond 111 DS ring visible on the detector, but a high strain sensitivity was ensured by this chosen geometry (Fig. 1). The data were used to generate plots of (i) intensity distribution $I_{111}(\theta, z)$ as a function of Bragg's angle θ and the sample depth z (denoted further as *phase plot*), (ii) intensity distribution $I_{111}(\delta, z)$ as a function of the DS ring azimuthal angle δ and the sample depth z (denoted further as *texture plot*) and (iii) to evaluate depth gradients of in-plane X-ray elastic strains $\varepsilon_{111}(z)$ for the diamond 111 reflection. In order to calculate residual stresses $\sigma(z)$ from the measured strains, the Hill grain interaction model was used for simplicity, with an X-ray elastic constant $0.5S_2$ of 9.38×10^{-9} Pa^{-1}. In order to correct the evaluated strain and stress values for the stress relaxation caused by the lamella preparation, a dedicated procedure based on a finite element model was applied [36]. Other details of the experimental approach and evaluation procedure can be found elsewhere [34,36].

2.3. Electron microscopy analysis

Scanning electron microscopy (SEM) analysis, electron backscatter diffraction (EBSD) and focused ion beam (FIB) machining/polishing on the NCD/PCD thin film cross-section was performed using a Zeiss AURIGA CrossBeam workstation. To obtain information on the film cross-sectional morphology, the cross-section was first polished by Ga ions by FIB within a 20 μm wide region followed by a final polishing step at a beam current of ~100 pA and an accelerating voltage of ~5 kV and under an angle of ~15° in order to achieve maximum smoothness and to remove residual impurities from previous coarser FIB milling. The EBSD characterisation with a lateral step of 50 nm was carried out with an Ametek-EDAX Hikari Super camera at an accelerating voltage of 20 kV and using a beam current of 6 nA, directly after the fine polishing in order to prevent contamination of the cross-section.

2.4. Hardness characterisation

The hardness of the individual sublayers was evaluated by nanoindentation, using a Hysitron TI950 Triboindenter on the same

Table 1
Summary of parameters used for the deposition of NCD and PCD sublayers on Si(100) substrate.

Substrate cleaning prior to the deposition	30 min in an Ar/H_2 plasma at 200 mbar with a microwave power of 1 kW (390 sccm Argon, 10 sccm H_2) at ~800 °C
Deposition temperature for NCD and PCD sublayers	800 and 900 °C
Deposition pressure	200 mbar
Microwave power	1 kW
Precursors for NCD	H_2/CH_4 (384 sccm H_2, 16 sccm CH_4)
Precursors for PCD	$Ar/H_2/CH_4$ plasma (386 sccm Ar, 10 sccm H_2, 4 sccm CH_4)
Deposition time	5 h for each sublayer

cross-section of the film that was prepared by FIB for the EBSD analysis. Ten indentation measurements were performed on the PCD and NCD sublayer cross-sections, approximately in the middle of each sublayer, and (for reference purposes) also on the underlying substrate. The measurements were carried out using a diamond Berkovich tip under quasi-static loading conditions, applying a maximum load of ~13 mN. They resulted in effective contact depths of ~60 nm for PCD and ~70 nm for NCD. The area function of the indenter tip was determined by reference measurements on fused silica. Recorded load-displacement data were evaluated according to the Oliver-Pharr method [37]. The hardness values (and corresponding standard errors) presented in Sec. 3 were calculated as the arithmetic mean of the results obtained from the ten individual measurements.

2.5. Micromechanical tests

In order to determine elastic moduli and fracture stresses of the CVD diamond multi-layer film, in-situ testing of micro-cantilevers and an evaluation procedure based on the classical linear-elastic theory of fracture mechanics were employed [39]. Eight micro-cantilevers with dimensions of ~$(1.4 \times 1.4 \times 12)$ μm^3 each were fabricated from the individual sublayers of the CVD diamond film using a FIB workstation (Zeiss AURIGA CrossBeam) (Fig. 2). Four cantilevers made from the coarse-grained top PCD sublayer were positioned about 2 µm beneath the sublayer surface. In order to access the NCD layer and to avoid the long FIB milling times, a large portion of PCD sublayer with a volume of ~$(200 \times 15 \times 30)$ μm^3 was removed using a femtosecond laser unit (Origami 10 XP) installed in the FIB workstation prior to the FIB machining. Four cantilevers were then milled approximately from the centre of the NCD sublayer. Details on the laser milling approach can be found in Ref. [38]. The FIB fabrication was performed using an acceleration voltage of ~30 kV and beam currents in the range from 20 nA to 50 pA. Special care was taken to avoid sample damage by Ga ions by using low FIB cutting currents at final cantilever machining steps.

All un-notched cantilever specimens were loaded and load-deflection curves were acquired. Micromechanical testing was carried out in in-situ configuration in a SEM (Zeiss LEO 982) by means of a dedicated indenter system Hysitron Pi-85 PicoIndenter, featuring a piezo-actuated sample stage. The cantilevers were loaded using a sphero-conical diamond indenter tip (with a radius of curvature of ~700 nm) in out-of-plane direction up to the load of fracture (Fig. 2). Testing was carried out at a constant displacement rate of ~20 nm/s in order to ensure quasi-static loading conditions. Special care was taken to load the cantilevers in their central planes to avoid torque. The load-deflection curves as well as the applied force were recorded and subsequently used to calculate Young's moduli.

Based on the recorded load-deflection data, fracture stress σ_s was evaluated as follows

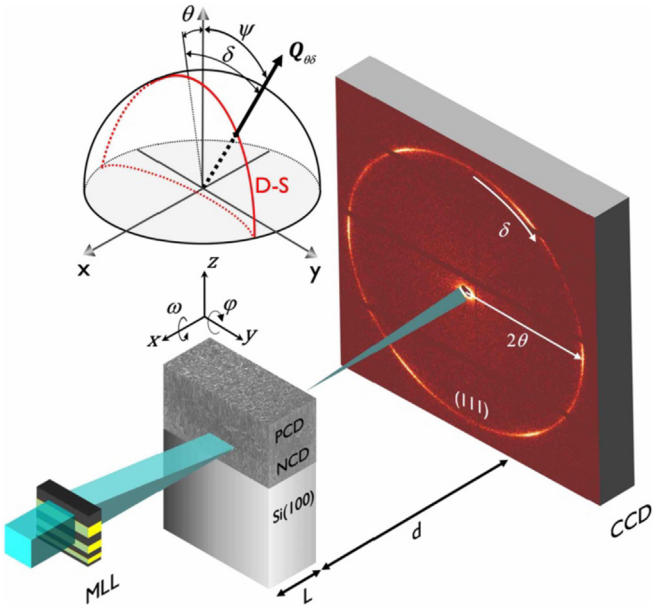

Fig. 1. A schematic drawing of the CSnanoXRD set-up at the ID13 beamline of ESRF in Grenoble. The experiment was performed in transmission diffraction geometry using one MLL to focus the synchrotron pencil X-ray beam (with $E = 13$ keV) to a cross-section of 15 µm × 30 nm. The sample lamella with a thickness L of ~100 µm comprising the multi-layered NCD/PCD thin film on Si(100) was scanned along the ***z*** direction in equidistant steps of 25 nm while the diffraction signal was recorded at every sample position by the 2D detector (Eiger X 4M) at a sample-to-detector distance d of ~125 mm. The azimuthal angle δ is counted from the 12 o'clock detector position and defined in clockwise direction as indicated on the detector plane schematically. (A colour version of this figure can be viewed online.)

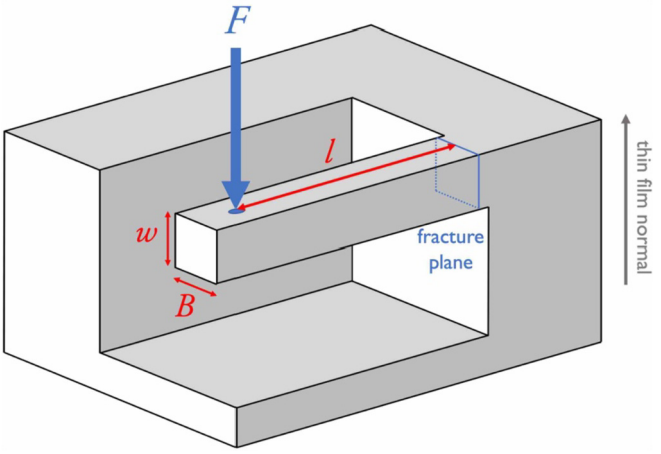

Fig. 2. A schematic drawing of the employed micro-cantilever specimen geometry indicating width B and thickness w. The bending length l is the distance between the point of the applied load F and the resulting fracture plane. (A colour version of this figure can be viewed online.)

$$\sigma_s = 6\frac{F\,l}{B\,w^2},$$

where F represents the maximum applied load at fracture, l is the bending length representing the distance between the point of the applied force and the resulting fracture plane, and B and w represent the cantilever width and thickness, respectively (Fig. 2). The evaluation of Young's modulus E rests on the assumption of an ideally brittle material, excluding plastic deformation effects of the tested material in contact with the indenter tip. The recorded dominant elastic response from cantilever loading is thus used to calculate E according to

$$E = \frac{4\,F}{\delta B} \times \left(\frac{l}{w}\right)^3,$$

δ being the displacement at maximum applied load F [39].

3. Results and discussion

3.1. Cross-sectional thin film morphology

The SEM micrograph from the NCD/PCD film fracture cross-section in Fig. 3 reveals a distinct two-layer architecture, with a very fine microstructure of the NCD base sublayer compared to the coarse-grained microstructure with prominent elongated columnar grains of the PCD sublayer. The interface between the sublayers is relatively sharp and flat, indicating small surface roughness of the NCD sublayer surface caused by its nanocrystalline nature. Measurements in the SEM on multiple fracture surfaces and cross-sections indicated an almost uniform film thickness of ~8 μm for NCD and ~14.5 μm for PCD sublayers.

The cross-sectional microstructure, grain morphology and crystallographic orientation of the grains were mapped by EBSD using a lateral step size of 50 nm. Fig. 4a presents an orientation map of the thin film cross-section for the film normal direction [001], while Fig. 4b shows an orientation map for the film in-plane direction [100]. The results document that the EBSD characterisation succeeded in determining the preferred orientation of the crystallites within the PCD sublayer only, indicating a ⟨110⟩ fibre texture. Additionally, the EBSD data from the PCD sublayer were used to generate three inverse pole figures for three perpendicular sample axes [100], [010] and [001], which correlate with two thin film in-plane (perpendicular and parallel to the micrograph plane) and one out-of-plane directions, respectively. The inverse pole figures (Fig. 4c) document, once more, the 110 fibre texture as well as a relatively regular in-plane orientation of crystallites with {111} planes oriented approximately perpendicular to the substrate surface.

The EBSD data (Fig. 4) together with the SEM micrograph from Fig. 3 indicate the presence of a Zone T type mechanism of competitive grain growth within the PCD sublayer. One can observe the columnar grain growth with selected grains stretching from the nucleation zone at the NCD/PCD interface to the film surface, whereas some other, smaller, grains close to the nucleation zone of the PCD sublayer cease to grow further after ~1–5 μm. In the case of the NCD sublayer, however, the EBSD approach failed to reveal the microstructure and preferred orientation of the nanocrystals, which is also apparent from Fig. 4b, where the NCD sublayer is entirely covered by the dark EBSD image quality. There, the low-quality EBSD signal can be explained by the small grain size of the crystallites of ~20 nm (cf. Sec. 3.2), which was close to, or somewhat below the resolution limit of the EBSD system.

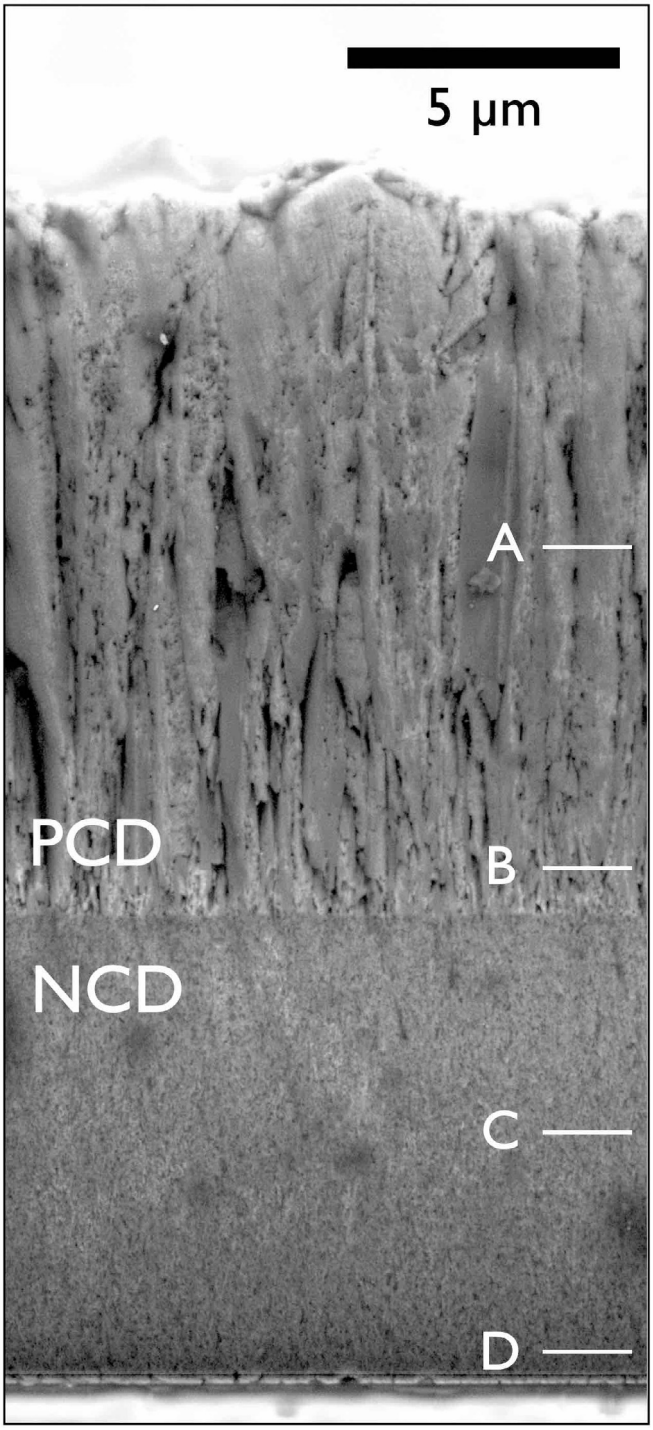

Fig. 3. SEM micrograph showing the cross-sectional morphology of the fine- and coarse-grained NCD and PCD sublayers, respectively. The markers at the cross-sectional positions A–D correspond approximately to the CSnanoXRD measurement positions, at which the DS rings in Fig. 5a were collected.

3.2. Synchrotron CSnanoXRD analysis

In Fig. 5a, four representative diamond 111 DS rings from the centre, the nucleation region of the PCD sublayer, as well as from the centre of the NCD sublayer and the corresponding nucleation region are presented (cf. also Fig. 3). They indicate a variation in texture across the film's thickness. In the NCD sublayer, the DS ring collected at position D (Fig. 5a) exhibits a relatively homogeneous

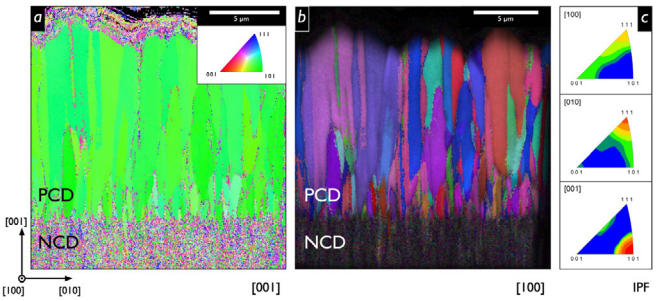

Fig. 4. EBSD [001] (a) and [100] (b) inverse pole figure (IPF) maps from a $20 \times 20\ \mu m^2$ cross-section of the NCD/PCD film indicating a columnar morphology of the microscopic diamond grains exhibiting a competitive grain growth mode in the PCD sublayer. The strip of noisy signal on top of the PCD films is artefacts stemming from the uneven sample surface. Crystallite size in NCD was below the resolution limit of the EBSD analysis. (c) EBSD [100], [010] and [001] inverse pole figures obtained from the data collected from the PCD sublayer, indicating the ⟨110⟩ fibre texture. (A colour version of this figure can be viewed online.)

azimuthal intensity distribution (nearly random texture), whereas azimuthal maxima at $\delta = 30°$ and 90° can be identified in the DS ring collected at position C. In the PCD sublayer, the azimuthal maxima of the DS rings taken at positions B and A become very pronounced. About 950 DS rings collected from the thin film cross-section were used to generate cross-sectional phase and texture plots $I_{111}(\theta, z)$ and $I_{111}(\delta, z)$, presented in Figs. 5b and 7, respectively.

The phase plot in Fig. 5b obtained by the azimuthal integration in the δ range of 80°–100° reveals an evolution of the diamond 111 reflection shape as a function of the film depth. In Fig. 5c, four representative diamond 111 reflections collected at the respective positions A–D (Figs. 3 and 5a) for the diffraction vector oriented approximately parallel to the substrate surface, are shown. In the NCD sublayer, the 111 reflections are broad and asymmetric with a shoulder at smaller diffraction angles, while in the PCD sublayer they become narrower. The phase plot (Fig. 5b) and the peak profiles corresponding to positions C and D from Fig. 5c with their asymmetric 111 reflection can be interpreted by the nanocrystalline and defect-rich nature of the NCD sublayer crystallites with a high stacking fault density. In contrast, the phase plot and the relatively narrow and symmetric line profiles corresponding to positions A and B from Fig. 5b and c indicate the presence of relatively large crystallites in the PCD sublayer.

The evolution of the XRD peak broadening was evaluated for all ~950 diamond 111 reflections for the in-plane orientation of the diffraction vector and is presented as full width at half maximum (*FWHM*) in Fig. 6. *FWHM* is usually sensitive to the size of coherently diffracting domains *D* and to the presence of crystal defects, resulting in the formation of strains of II and III order. The *FWHM* data from Fig. 6 are shown together with the *D* obtained by Scherrer's equation $D \cong \lambda/(FWHM \cdot \cos\theta)$, using the beam wavelength $\lambda = 0.9537$ Å and neglecting strain-induced broadening for the sake of simplicity. The results indicate that the in-plane crystallite size is smallest in the NCD sublayer at the interface to Si(100), reaching values below 20 nm, then increases to ~24 nm within the 1.5 μm thick nucleation layer before saturating and remaining relatively unchanged. Within the PCD sublayer, the average in-plane crystallite size increases from about 40 nm to 60 nm and remains constant across the entire sublayer.

The texture plot $I_{111}(\delta, z)$ in Fig. 7 shows the gradual evolution of texture across the film's cross-section. At the interface to the Si(100) substrate, the crystallites are oriented randomly in the NCD sublayer (cf. also Fig. 5a). Starting at a thickness of ~1.5 μm, the ⟨110⟩ fibre texture starts to evolve within the NCD sublayer and becomes sharper towards the NCD/PCD interface. Across the PCD sublayer, the 110 texture is also becoming stronger towards the surface, due to the mechanism of competitive columnar grain growth discussed in Sec. 3.1. One important feature of the ⟨110⟩ fibre texture is the presence of distinct azimuthal maxima at $\delta = 90°$ and 180°, which represent the diffraction on {111} crystallographic planes oriented approximately perpendicular to the substrate surface, with diffraction vectors oriented parallel to the surface. The CSnanoXRD data are in agreement with the EBSD data (Fig. 4), confirming the texture type for the PCD sublayer and complementing the missing data for the NCD sublayer.

CSnanoXRD was employed to evaluate gradients of X-ray elastic strain $\varepsilon_{111}(z)$ and in-plane biaxial residual stress across the film thickness. The acquired strains and stresses presented in Fig. 8 document the presence of complex gradients. The highest stress of ~1.1 GPa was observed in the NCD sublayer at the interface to the Si(100) substrate. Within the NCD sublayer nucleation region, these tensile stresses were observed to drop rapidly to about 750 MPa,

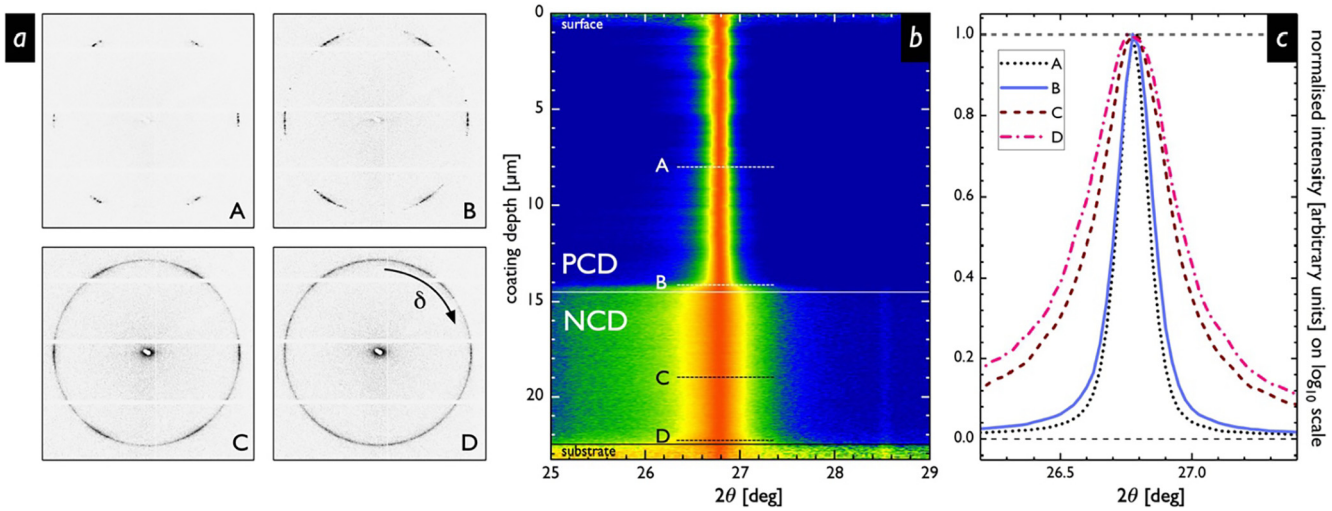

Fig. 5. (a) DS rings collected from the PCD and NCD sublayers at the cross-sectional positions A–D (cf. Fig. 3) indicate a variation of texture across the film. (b) Phase plot $I_{111}(\delta, z)$ obtained by azimuthal integration of about 950 DS rings in the δ range of 80°–100°. (c) Normalised intensity distributions of exemplary diamond 111 reflections, representing diffraction on diamond {111} crystallographic planes oriented perpendicular to the substrate surface, collected at positions A–D. (A colour version of this figure can be viewed online.)

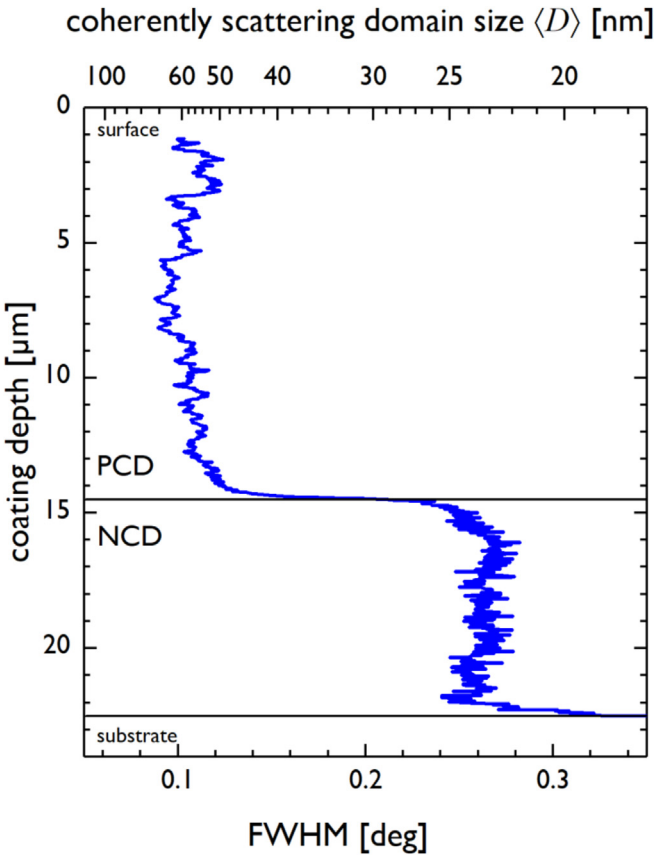

Fig. 6. Cross-sectional evolution of *FWHM* of the diamond 111 reflection evaluated from DS rings for $\delta = 90°$, corresponding to the in-plane orientation of the diffraction vectors, and the linked in-plane size of coherently scattering domains *D* obtained from Scherrer's equation. (A colour version of this figure can be viewed online.)

and then found to decrease linearly towards the NCD/PCD sublayer interface, where the stress state switches to compressive. Across the PCD sublayer, the stress state changes very locally and overall becomes tensile again towards the surface. These abrupt changes in stress within the PCD sublayer can be attributed to the coarse-grained nature of this sublayer as well as varying stress states within individual grains. It is obvious that the observed stress variation across the diamond thin film cross-section can be correlated with intrinsic stress changes caused by the complex microstructure evolution (cf. Sec. 4).

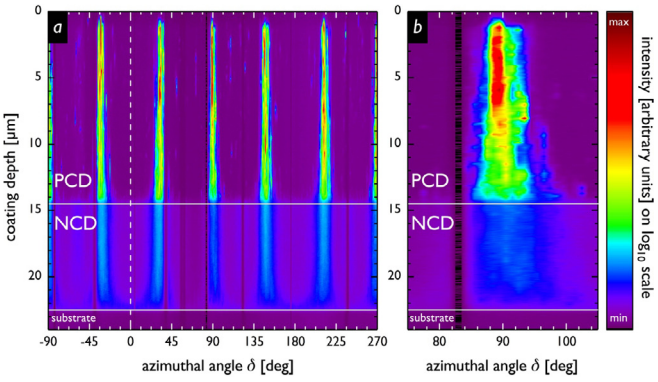

Fig. 7. Texture plot $I_{111}(\delta, z)$ obtained by radial integration of ~950 DS rings showing the cross-sectional texture evolution for the entire azimuthal range (a), and for a selected azimuthal range around 90° (b). (A colour version of this figure can be viewed online.)

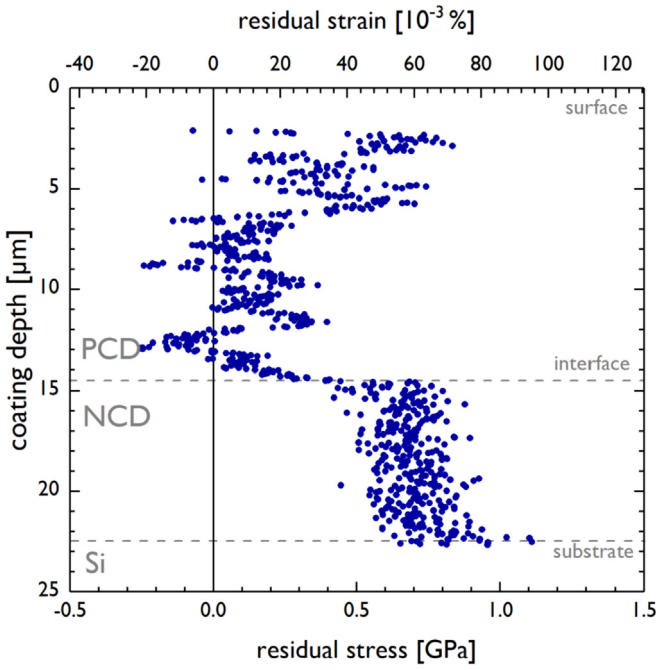

Fig. 8. Gradient of residual stress and X-ray elastic strains $\varepsilon_{111}(z)$ across the film depth determined using CSnanoXRD. (A colour version of this figure can be viewed online.)

3.3. Cross-sectional mechanical properties of the sublayers

In Fig. 9a, SEM micrographs of micro-cantilevers machined using FIB from the NCD (four specimens plus one pre-test) and PCD (four specimens) sublayers are presented together with the micrographs of two representative cantilever specimens in Fig. 9b and c, respectively. The load-deflection curves recorded during the bending experiments on both types of cantilevers presented in

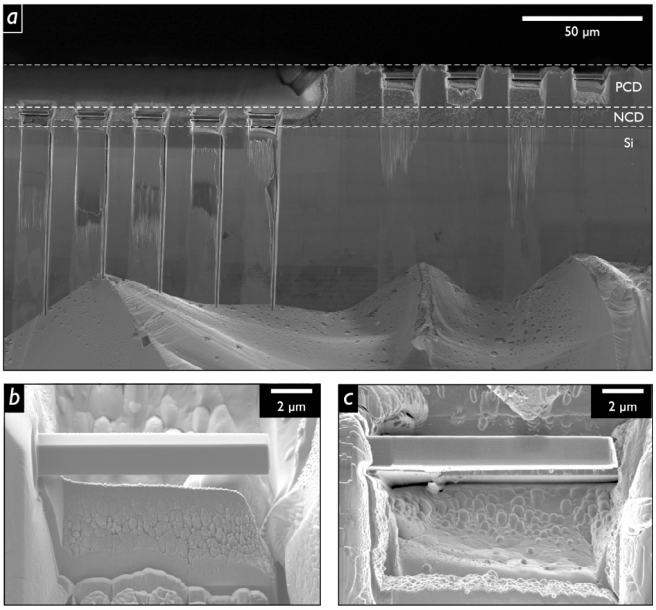

Fig. 9. SEM micrographs of five (four plus one specimen for pre-testing) and four micro-cantilevers machined from the NCD and PCD sublayers (a) together with the magnified micrographs of representative cantilevers from PCD (b) and NCD (c) sublayers. The approaching sphero-conical diamond indenter tip is visible in the upper part of micrograph (c).

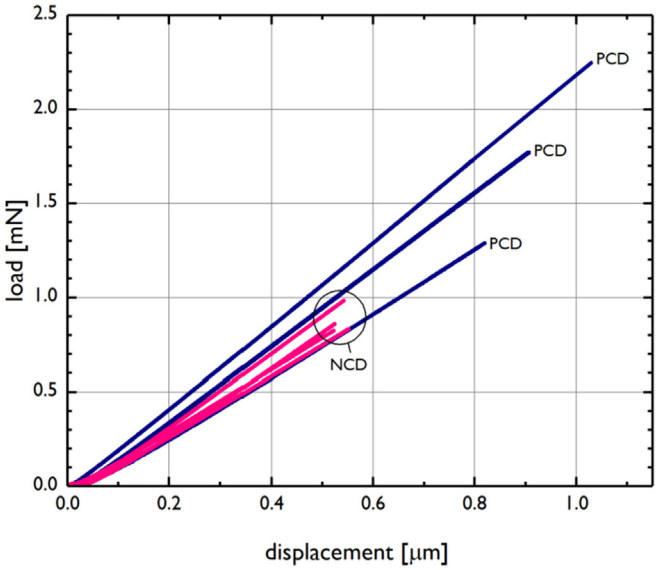

Fig. 10. Load-deflection curves recorded during bending experiments on micro-cantilevers (Fig. 9) machined from the NCD and PCD sublayers, indicating the comparatively smaller Young's modulus and fracture stress of the NCD sublayer. (A colour version of this figure can be viewed online.)

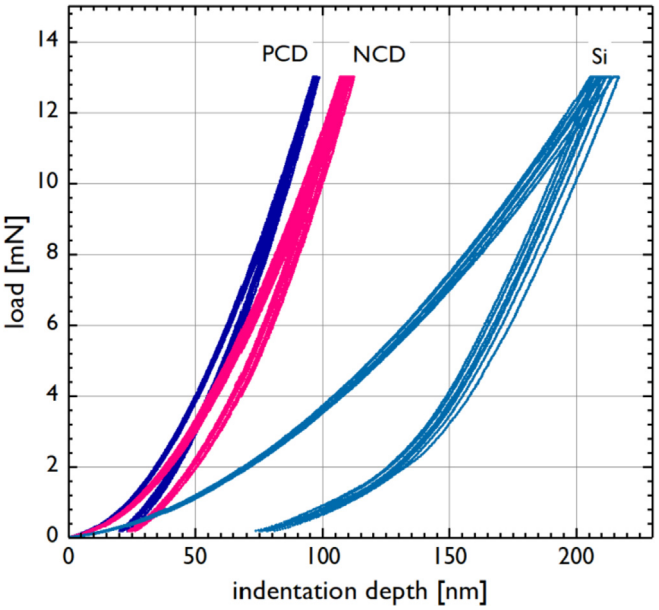

Fig. 11. Load-displacement curves recorded during cross-sectional indentation experiments on the NCD and PCD sublayers, indicating the smaller Young's modulus and hardness of the NCD sublayer. The response of the Si substrate is shown for reference. (A colour version of this figure can be viewed online.)

Fig. 10 show linear elastic behaviour, i.e. the cantilevers behaved like an ideal bending beam and broke without detectable plastic and/or ductile response [39]. The data set of one micro-cantilever from the PCD sublayer showed unrealistic load-deflection characteristics. It was treated as an outlier, disregarded from further evaluation and is not shown in Fig. 10. The distinct differences in the slopes and in the (maximum) loads at fracture between the curves from the NCD and PCD type cantilevers (Fig. 10) qualitatively indicate the differences in the mechanical properties of the sublayers. The recorded micromechanical data from the cantilevers were used to evaluate fracture stresses and Young's moduli (cf. Sec. 2), of which the mean averages are presented in Table 2. The quantitative data document a difference of ~10% in the Young's moduli and a significant difference in the fracture stresses between the sublayers, which are both discussed in Sec. 4.

In addition, the hardness of the NCD and PCD sublayers was determined by means of nanoindentation performed on the sublayers' cross-sections. In Fig. 11, thirty load-displacement responses are presented, ten from each of the NCD and PCD sublayers' as well as the underlying Si substrate's cross-sections. Again, the differences between the slopes and the maximal penetration depths (Fig. 11) indicate qualitative differences in the mechanical properties of both sublayers. The recorded indentation data were used to determine the hardness of the sublayers presented in Table 2.

4. Discussion of cross-sectional correlations

As discussed in Sec. 1, the physical properties of CVD diamond thin films depend on cross-sectional microstructure and stress gradients, which evolve as a function of the deposition conditions, in particular as a result of the applied process parameters as well as of a variety of self-organisation phenomena taking place at distinct stages of the growth process. In this section, the correlations between (i) the observed phenomena and (ii) the methodological aspects of the applied correlative cross-sectional nano-analytics approach will be discussed.

Table 2
Mechanical properties of the NCD and PCD sublayers evaluated by bending experiments on micro-cantilevers and cross-sectional indentation tests.

	Fracture stress σ_s[GPa]	Young's modulus E [GPa]	Hardness [GPa]
PCD sublayer	31.6 ± 6.6	1037 ± 25.3	60.8 ± 0.9
NCD sublayer	14.3 ± 0.6	903 ± 35.3	46.5 ± 1.7

Electron microscopy and diffraction (SEM, EBSD) as well as CSnanoXRD (Figs. 3,5–8) revealed the presence of a nanocrystalline nucleation region in the NCD sublayer with a thickness of ~1.5 μm, possessing the highest tensile stress of ~1.1 GPa at the interface to Si(100) and showing the smallest apparent in-plane crystallite size D of ~18 nm and random texture. This observation is in agreement with the model of Silva et al. [8], where it was proposed that the growth of ballas-like crystallites composed of nanometric sectors elongated along the [110] axes results in the formation of a ⟨110⟩ fibre texture. At a thicknesses of ~1.5–8 μm, both microstructure and stress evolution become saturated within the NCD sublayer as a result of steady state grain growth conditions, resulting in a tensile stress level of 0.75 GPa and a crystallite size D of ~24 nm, while the ⟨110⟩ texture sharpness changes only marginally. The presence of the near-substrate transition region with random nucleation texture lacking significant growth competition in the early growth stage correlates with the experimental results and texture models reported from other thin monolithic films [5,7,8]. It is, however, interesting to observe that the transition from the nucleation regime during the NCD sublayer formation occurs very abruptly.

EM and CSnanoXRD (Figs. 3–8) also revealed the presence of a transition region with a thickness of ~2 μm within the PCD sublayer. At a total film thickness of ~8–10 μm, one can observe a decrease in stress from 0.7 to −0.3 GPa, a further sharpening of ⟨110⟩ texture, as well as an increase in crystallite size D from ~25 to ~50 nm. The presence of this transition region within the PCD sublayer can also be identified in the EBSD inverse pole figure orientation maps (Fig. 4a and b), indicating competitive columnar grain growth, which ceases after about 2–2.5 μm. At a thickness of ~10–22.5 μm, the microstructure evolution becomes saturated within the PCD

sublayer as a result of stable grain growth conditions. The variation in tensile stress across the PCD sublayer can be interpreted by the large size of the diamond crystallites, of which the analysis using the X-ray nanoprobe provided just very local information on the stress state. If the sampling volume were significantly larger, encompassing a much higher number of grains, the local stress variations would average out and result in a smoother stress profile, akin to that found in the NCD sublayer.

The significant differences between the sublayers' observed intrinsic microstructural characteristics can be attributed to different deposition conditions applied during the synthetises of the NCD and PCD sublayers. Especially the lower deposition temperature of ~800 °C and the application of the $Ar/H_2/CH_4$ plasma played an important role in the formation of the nanocrystalline bottom (NCD) sublayer. The temperature difference of ~100 °C in conjunction with two different types of plasma environments resulted in the formation of sublayers with profoundly distinct microstructural attributes. Interestingly however, in both sublayers, the presence of nucleation transition regions was detected by EM and CSnanoXRD. Within the transition regions all microstructural parameters such as texture, crystallite size, stress, and grain boundaries change rapidly before they reach a saturation state. The NCD and PCD sublayers exhibit different levels of residual stress of ~0.75 and 0.25 GPa (Fig. 8), which after adding the thermal stress component of ~ -0.72 and −0.81 GPa [12,13,15], indicate tensile growth stresses of 1.4 and 1 GPa, respectively. The difference in the growth stresses can be interpreted by the sublayers' microstructure. In particular, the larger portion of grain boundaries in the nanocrystalline base sublayer could be responsible for generating larger tensile growth stress as a result of the coalescence of columnar grain boundaries during the initial stages of the sublayer growth [7,8].

The cross-sectional microstructure can be correlated with the mechanical properties of the sublayers, which were characterised using cross-sectional indentation and micro-cantilever bending experiments (Table 2). In general, the mechanical characterisation indicated significantly smaller hardness, fracture stress and Young's modulus for the NCD sublayer, compared to the PCD sublayer, which can be attributed to the nanocrystalline nature of the bottom sublayer, with small crystallites and a comparatively large volume fraction of grain boundaries. The obtained quantitative results of hardness and Young's moduli presented in Table 2 are in agreement with the results obtained from monolithic nanocrystalline and polycrystalline diamond thin films [26]. In the case of fracture stress, however, significantly larger values of 14.3 ± 0.6 and 31.6 ± 6.6 GPa were determined using the micro-cantilever bending method. These values appear significantly larger than the data evaluated from other diamond samples (cf. Fig. 4 in Ref. [26]), especially compared to the tensile strength data of 5.2 GPa from Olson et al. [40]. Compared to the data from micromechanical compressive tests on diamond single crystals [27], however, the obtained fracture stress values appear very reasonable and document the discrepancy between tensile and compressive strengths in diamond. In addition, the present data also indicate the advantage of the micro-cantilever approach. Unfortunately, it was not possible to perform a mechanical characterisation of the nucleation regions of the NCD and PCD sublayers, which would require further downscaling of the micromechanic specimens.

One important novelty of this work is the application of a *correlative cross-sectional nanoanalytics approach* to the investigated multi-layered NCD/PCD thin film. The combination of EM and CSnanoXRD allowed for obtaining quantitative experimental data on the cross-sectional evolution of microstructure and stress. These approaches were found to be quite complementary: while it was not possible to determine texture gradients in the NCD sublayer by means of EBSD analysis, CSnanoXRD allowed for obtaining very local information on texture gradient across the nanocrystalline transition nucleation region. The first application of CSnanoXRD to a diamond thin film demonstrated the possibilities of the technique to study depth gradients of microstructure and stress in both nanocrystalline and coarse-grained thin films. In order to obtain cross-sectional structure-property correlations for diamond thin films, the combination of EM and CSnanoXRD techniques on one side, and of cross-sectional micromechanical characterisation on the other represents a great methodological advance. There remains, however, the need to improve the spatial resolution of the mechanical tests.

5. Conclusions

In this work, a novel *correlative cross-sectional nano-analytics approach* was used to characterise cross-sectional structure-property relationships in a multi-layered CVD diamond film grown using microwave plasma-enhanced CVD and consisting of a ~8 μm thick nanocrystalline (NCD) bottom and a ~14.5 μm thick polycrystalline (PCD) top diamond sublayer. For the characterisation, depth-resolved micro-cantilever and hardness testing, electron microscopy methods and novel CSnanoXRD were applied. CSnanoXRD was used for the first time to study properties of diamond thin film. The cross-sectional experimental data revealed complex correlations between thin film mechanical properties, texture, crystallite size, residual stresses and deposition conditions. The fine-grained NCD and coarse-grained columnar PCD sublayers indicated the presence of nucleation regions with distinct gradual microstructures, which were investigated primarily by CSnanoXRD. The values of hardness and Young's moduli from both sublayers correlate well with the results reported from other monolithic CVD diamond thin films, whereas relatively large fracture stresses were observed using the micro-cantilever method. The presence of the gradual microstructures and stress gradients, however, documents the importance of the cross-sectional analysis, which should be further developed and downscaled. In summary, the nano-analytics approach allows for understanding the correlation between deposition conditions, cross-sectional gradients of microstructure, residual stress and mechanical properties and overall functional properties of diamond thin films.

Acknowledgement

The authors gratefully acknowledge the financial support under the scope of the COMET program within the K2 Centre “Integrated Computational Material, Process and Product Engineering (IC-MPPE)” (Project No. 859480). This program is supported by the Austrian Federal Ministries for Transport, Innovation and Technology (BMVIT) and for Digital and Economic Affairs (BMDW), represented by the Austrian research funding association (FFG), and the federal states of Styria, Upper Austria and Tyrol. This work was carried out with the support of CEITEC Nano Research Infrastructure (ID LM2015041, MEYS CR, 2016–2019), CEITEC Brno University of Technology.

References

[1] P.W. May, Diamond thin films: a 21st-century material, Philos. Trans. R. Soc. A Math. Phys. Eng. Sci. 358 (2000) 473–495.
[2] O.A. Williams, Nanocrystalline diamond, Diam. Relat. Mater. 20 (2011) 621–640.
[3] F. Celii, J.E. Butler, Diamond chemical vapor deposition, Annu. Rev. Phys. Chem. 42 (1991) 643–684.
[4] O. Auciello, A.V. Sumant, Status review of the science and technology of ultrananocrystalline diamond (UNCD™) films and application to multifunctional devices, Diam. Relat. Mater. 19 (2010) 699–718.

[5] A. Van Der Drift, Evolutionary selection, a principle governing growth orientation in vapour-deposited layers, Philips Res. Rep. 22 (1967) 267–288.
[6] C. Wild, N. Herres, P. Koidl, Texture formation in polycrystalline diamond films, J. Appl. Phys. 68 (1990) 973–978.
[7] T. Liu, D. Raabe, W.M. Mao, A review of crystallographic textures in chemical vapor-deposited diamond films, Signal. Front. Mater. Sci. China 4 (2010) 1–16.
[8] F. Silva, F. Bénédic, P. Bruno, A. Gicquel, Formation of(110) texture during nanocrystalline diamond growth: an X-ray diffraction study, Diam. Relat. Mater. 14 (3–7) (2005) 398–403.
[9] W. Kulisch, C. Popov, On the growth mechanisms of nanocrystalline diamond films, Phys. Status Solidi 203 (2006) 203–219.
[10] K.J. Sankaran, B.R. Huang, A. Saravanan, D. Manoharan, N.H. Tai, I.N. Lin, Nitrogen incorporated ultrananocrystalline diamond microstructures from bias-enhanced microwave N_2/CH_4-plasma chemical vapor deposition, Plasma Process. Polym. 13 (4) (2016) 419–428.
[11] C. Kirchlechner, K.J. Martinschitz, R. Daniel, C. Mitterer, J. Keckes, Residual stresses in thermally cycled CrN coatings on steel, Thin Solid Films 517 (2008) 1167–1171.
[12] N. Woehrl, T. Hirte, O. Posth, V. Buck, Investigation of the coefficient of thermal expansion in nanocrystalline diamond films, Diam. Relat. Mater. 18 (2–3) (2009) 224–228.
[13] J. Michler, M. Mermoux, Y. Von Kaenel, A. Haouni, G. Lucazeau, E. Blank, Residual stress in diamond films: origins and modelling, Thin Solid Films 357 (2) (1999) 189–201.
[14] J.G. Kim, J. Yu, A study on the residual stress measurement methods on chemical vapor deposition diamond films, J. Mater. Res. 13 (1998) 3027–3033.
[15] H. Li, B.W. Sheldon, A. Kothari, Z. Ban, B.L. Walden, Stress evolution in nanocrystalline diamond films produced by chemical vapor deposition, J. Appl. Phys. 100 (2006), 094309.
[16] M. Mohr, L. Daccache, S. Horvat, K. Brühne, T. Jacob, H.J. Fecht, Influence of grain boundaries on elasticity and thermal conductivity of nanocrystalline diamond films, Acta Mater. 122 (2017) 92–98.
[17] C. Hua, X. Yan, J. Wei, J. Guo, J. Liu, L. Chen, L. Hei, C. Li, Intrinsic stress evolution during different growth stages of diamond film, Diam. Relat. Mater. 73 (2017) 62–66.
[18] H. Windischmann, G.F. Epps, Y. Cong, R.W. Collins, Intrinsic stress in diamond films prepared by microwave plasma CVD, J. Appl. Phys. 69 (1991) 2231.
[19] M. Hempel, M. Härting, Characterisation of CVD grown diamond and its residual stress state, Diam. Relat. Mater. 8 (8–9) (1999) 1555–1559.
[20] R.S. Balmer, J.R. Brandon, S.L. Clewes, H.K. Dhillon, J.M. Dodson, I. Friel, P.N. Inglis, T.D. Madgwick, M.L. Markham, T.P. Mollart, N. Perkins, G.A. Scarsbrook, D.J. Twitchen, A.J. Whitehead, J.J. Wilman, S.M. Woollard, Chemical vapour deposition synthetic diamond: materials, technology and applications, J. Phys. Condens. Matter 21 (36) (2009) 364221.
[21] J. Philip, P. Hess, T. Feygelson, J.E. Butler, S. Chattopadhyay, K.H. Chen, L.C. Chen, Elastic, mechanical, and thermal properties of nanocrystalline diamond films, J. Appl. Phys. 93 (2003) 2164.
[22] M. Mohr, A. Caron, P. Herbeck-Engel, R. Bennewitz, P. Gluche, K. Brühne, H.J. Fecht, Young's modulus, fracture strength, and Poisson's ratio of nanocrystalline diamond films, J. Appl. Phys. 116 (2014) 124308.
[23] O.A. Williams, A. Kriele, J. Hees, M. Wolfer, W. Müller-Sebert, C.E. Nebel, High young's modulus in ultra thin nanocrystalline diamond, Chem. Phys. Lett. 495 (1–3) (2010) 84–89.
[24] H.D. Espinosa, B. Peng, N. Moldovan, T.A. Friedmann, X. Xiao, D.C. Mancini, O. Auciello, J. Carlisle, C.A. Zorman, M. Merhegany, Elasticity, strength, and toughness of single crystal silicon carbide, ultrananocrystalline diamond, and hydrogen-free tetrahedral amorphous carbon, Appl. Phys. Lett. 89 (2006), 073111.
[25] F.S. Kachold, M.A. Lodes, S.M. Rosiwal, R.F. Singer, Direct measurement of Young's modulus, fracture strength and fracture toughness of nanocrystalline diamond foil by means of tensile testing, Acta Mater. 61 (2013) 7000–7008.
[26] P. Hess, The mechanical properties of various chemical vapor deposition diamond structures compared to the ideal single crystal, J. Appl. Phys. 111 (2012), 051101.
[27] J.M. Wheeler, R. Raghavan, J. Wehrs, Y. Zhang, R. Erni, J. Michler, Approaching the limits of strength: measuring the uniaxial compressive strength of diamond at small scales, Nano Lett. 16 (2016) 812–816.
[28] J.E. Butler, A.V. Sumant, The CVD of nanodiamond materials, Chem. Vap. Depos. 14 (2008) 145–160.
[29] M. Wiora, K. Brühne, A. Flöter, P. Gluche, T.M. Willey, S.O. Kucheyev, A.W. Van Buuren, A.V. Hamza, J. Biener, H.-J. Fecht, Grain size dependent mechanical properties of nanocrystalline diamond films grown by hot-filament CVD, Diam. Relat. Mater. 18 (2009) 927–930.
[30] X. Li, D. Diao, B. Bhushan, Fracture mechanisms of thin amorphous carbon films in nanoindentation, Acta Mater. 67 (1997) 4453–4461.
[31] C.S. Pickles, The fracture stress of chemical vapour deposited diamond, Diam. Relat. Mater. 11 (2002) 1913–1922.
[32] K. An, L. Chen, X. Yan, X. Jia, J. Liu, J. Wei, Y. Zhang, F. Lu, C. Li, Fracture strength and toughness of chemical-vapor-deposited polycrystalline diamond films, Ceram. Int. 44 (2018) 17845–17851.
[33] J. Keckes, M. Bartosik, R. Daniel, C. Mitterer, G. Maier, W. Ecker, J. Vila-Comamala, C. David, S. Schoeder, M. Burghammer, X-ray nanodiffraction reveals strain and microstructure evolution in nanocrystalline thin films, Scripta Mater. 67 (2012) 748–751.
[34] J. Keckes, R. Daniel, J. Todt, J. Zalesak, B. Sartory, S. Braun, J. Gluch, M. Rosenthal, M. Burghammer, C. Mitterer, S. Niese, A. Kubec, 30 nm X-ray focusing correlates oscillatory stress, texture and structural defect gradients across multilayered TiN-SiO_x thin film, Acta Mater. 144 (2018) 862–873.
[35] J. Kieffer, D. Karkoulis, PyFAI, a versatile library for azimuthal regrouping, J. Phys. Conf. Ser. 425 (2013) 202012.
[36] M. Stefenelli, J. Todt, A. Riedl, W. Ecker, T. Müller, R. Daniel, M. Burghammer, J. Keckes, X-ray analysis of residual stress gradients in TiN coatings by a Laplace space approach and cross-sectional nanodiffraction: a critical comparison, J. Appl. Crystallogr. 46 (2013) 1378–1385.
[37] W.C. Oliver, G.M. Pharr, Measurement of hardness and elastic modulus by instrumented indentation: advances in understanding and refinements to methodology, J. Mater. Res. 19 (2004) 3–20.
[38] M.J. Pfeifenberger, M. Mangang, S. Wurster, J. Reiser, A. Hohenwarter, W. Pfleging, D. Kiener, R. Pippan, The use of femtosecond laser ablation as a novel tool for rapid micro-mechanical sample preparation, Mater. Des. 121 (2017) 109–118.
[39] K. Matoy, H. Schönherr, T. Detzel, T. Schöberl, R. Pippan, C. Motz, G. Dehm, A comparative micro-cantilever study of the mechanical behavior of silicon based passivation films, Thin Solid Films 518 (2009) 247–256.
[40] D.S. Olson, G.J. Reynolds, G.F. Virshup, F.I. Friedlander, B.G. James, L.D. Partain, Tensile strength of synthetic chemical-vapor-deposited diamond, J. Appl. Phys. 78 (1995) 5177–5179.